

# Creation and Interaction of Dark and Bright Topological Breathers from Soliton-Cnoidal Wave Collisions

Yifeng Mao,<sup>1,\*</sup> Sathyanarayanan Chandramouli,<sup>2</sup> Wenqian Xu,<sup>1</sup> and Mark Hoefer<sup>1</sup>

<sup>1</sup>*Department of Applied Mathematics, University of Colorado, Boulder, CO 80309, USA*

<sup>2</sup>*Department of Mathematics, Florida State University, Tallahassee, FL 32306, USA.*

(Dated: February 23, 2023)

Two families of topological breathers are created in a core-annular flow system by interacting a soliton and a nonlinear periodic (cnoidal) carrier. Bright and dark breathers are observed to move faster or slower, respectively, than the carrier while imparting a topological phase shift. Agreement with weakly nonlinear exact solutions and numerical simulations of a strongly nonlinear model is achieved. Collisions within and across breather families are observed to be elastic. The breather creation method and breather properties are expected to generalize to many continuum and discrete systems.

Breathers are spatially (or temporally) localized, periodic in time (or space) disturbances in the comoving frame. They generalize classical solitons by incorporating two time scales: one associated with propagation and the other associated with internal oscillations. Perhaps the most prevalent physical systems where breathers play a fundamental role are in water waves and fiber optics. For example, breathers in the weakly nonlinear regime are envelope solitary waves involved in energy transport [1–4], ship wave generation [5], internal waves resulting from Earth’s rotation [6], and optical communications [7]. Breathers are also identified with rogue waves [8–12] and the far-from-equilibrium dynamics of many-breather interactions has led to the burgeoning field of integrable turbulence and breather gases [13–17]. But breathers are not limited to optics and water waves as they are also fundamental nonlinear excitations in magnetic materials [18, 19], ultracold atomic gases [20, 21], and discrete systems [22–24].

Breathers can be divided into classes based on their polarity and whether or not they are topological. A breathers’ polarity is determined by the disturbance type. If it is a wave of elevation, then it is called a bright breather (BB), whereas a depression wave is a dark breather (DB). The most well-known BBs are the bright envelope solitons in optical fibers [25], deep water waves [26], and spin waves [19], which propagate on a uniform background. An inhomogeneous, periodic background such as the shallow water cnoidal wave modeled by the Korteweg-de Vries (KdV) equation can also support breather propagation, where it is interpreted spectrally as the superposition of an eigenvalue (soliton) and spectral bands (cnoidal wave) within inverse scattering theory (IST) [27–29]. A breather is topological if it propagates on a carrier, e.g., cnoidal, wave and imparts a nonzero phase shift. All DBs necessarily exhibit topology, the most well-known being the dark envelope soliton [4, 30], while most if not all observed BBs are non-topological [5–7, 20, 21, 23]. Breather theory has emphasized the weakly nonlinear regime encapsulated by the

nonlinear Schrödinger equation (NLS) approximation, possessing dark soliton (topological DB) or bright soliton (non-topological BB) solutions in the defocusing or focusing case, respectively [31], or few-cycle non-topological BBs modeled by the modified KdV (mKdV) equation or the mKdV-sine-Gordon equation [32, 33]. However, the experimental confirmation of the existence, characterization, and interaction of strongly nonlinear, topological BBs and DBs in the same physical system is lacking.

In this Letter, we create and interact strongly nonlinear, topological BBs and DBs at the interface between two viscous fluids by the overtaking interaction of a carrier wave with a soliton or vice-versa, proving that this class of breathers can be interpreted as a nonlinear superposition between a soliton and a carrier or cnoidal-like wave. We measure their properties during free propagation and interaction, finding that they retain their topological and solitonic character, i.e., interactions are elastic. Qualitative and quantitative features of individual breathers and their interactions agree with recent predictions from KdV breather theory [28, 29] and numerical simulations of a strongly nonlinear model, respectively. We physically realize the spectral interpretation of a breather from IST. Increasing breather speeds imply decreasing (BB) or increasing (DB) carrier phase shifts. Unimodal and bimodal geometries of internal oscillation are observed. Slower (faster) breathers exhibit a negative (positive) spatial shift post-interaction. The method of breather generation and their characterization are relevant for the physics of nonlinear dispersive media writ large.

The experiments are conducted in a tall acrylic column of 5cm × 5cm × 180cm, described in [34]. The column consists of a pressure-driven viscous core fluid with a free interface to a miscible, heavier viscous reservoir fluid with a small core-to-reservoir fluid viscosity ratio. We precisely control the injection of the buoyant, interior fluid in the low Reynolds number regime, which is convectively unstable [35, 36], so that straight conduits are established with constant injection. Time-varying injection

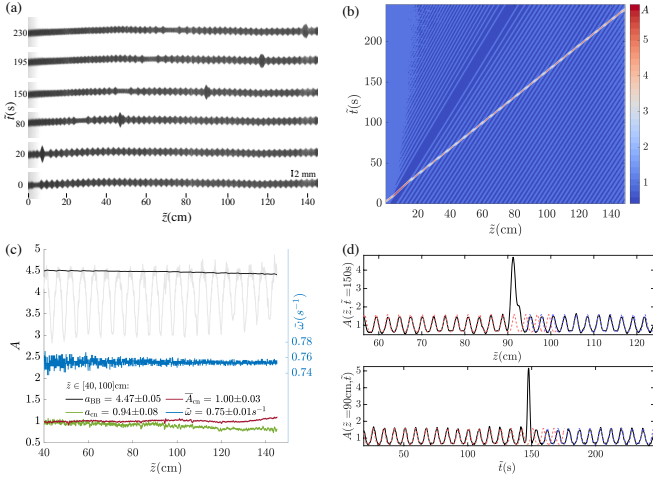


FIG. 1. Bright breather (BB) in a viscous fluid conduit formed from a soliton overtaking a cnoidal-like periodic traveling wave. (a) 90° clockwise rotated time-lapse. (b) Space-time contour of the cross-sectional area. (c) Background cnoidal-like wave and BB measurements at different heights. (d) Spatial and temporal profiles (black solid) and the cnoidal-like wave solution of the conduit equation (1) corresponding to measured parameters (dashed).

results in a conduit that exhibits an azimuthally symmetric interface with cross-sectional area  $A(z, t)$ , where  $z > 0$  is the vertical spatial coordinate in the camera view that is slightly above the injection site. We identify  $t = 0$  as the time at the initiation of interfacial imaging. At the injection site, the cross-sectional area satisfies the Hagen-Poiseuille flow law  $Q \propto A^2$  so it can be precisely controlled by temporally varying the injection rate  $Q$  [37, 38].

Viscous core-annular interfacial waves are modeled by the strongly nonlinear conduit equation [38, 39]

$$A_t + (A^2)_z - (A^2 (A^{-1} A_t))_z = 0, \quad (1)$$

given in non-dimensional form where  $z = \tilde{z}/L$ ,  $t = \tilde{t}/T$ ,  $A = \tilde{A}/A_0$  for dimensional quantities  $\tilde{z}$ ,  $\tilde{t}$ ,  $\tilde{A}$  and  $L$ ,  $T$ ,  $A_0$  are the fitted vertical length, time, and cross-sectional area, respectively, obtained from separate measurements of linear dispersive waves on the background injection rate  $Q_0 \propto A_0^2$  [40]. Cnoidal-like waves in the form  $A(z, t) = g(\theta)$ ,  $\theta = kz - \omega t$ ,  $g(\theta + 2\pi) = g(\theta)$  and solitons are generated by evaluating numerically computed traveling wave solutions of the conduit equation [41] at the injection site, which determines the injection rate time-series  $Q(t) \propto g(-\omega t)^2$ . The characterization and reliable generation of soliton and cnoidal-like waves have, individually, been reported in [34, 38, 42].

Figure 1 displays the spatio-temporal evolution of a soliton overtaking a cnoidal-like wave. At  $t = 0$ , we have prepared the conduit as a nonlinear cnoidal-like wave (the *carrier*) that abruptly terminates at the injection site to a constant flow rate for  $t > 0$ . The carrier propagates up-

ward for positive  $z$  and experiences a modulation region as it transitions from periodic to a constant background (Fig. 1a for  $t > 20\text{s}$ , Fig. 1b) [40]. This modulated region consists of a dispersive shock wave (DSW) [43], a constant region whose value  $A_{\min}$  coincides with the minimum of the adjacent carrier, and a carrier modulation [43, 44]. The averaged carrier's amplitude ( $a_{\text{cn}}$ ), mean ( $\bar{A}_{\text{cn}}$ ), and dimensional phase frequency ( $\tilde{\omega} = \omega/T$ ) are reported in Fig. 1c. The measured wavenumber ( $\tilde{k} = k/L$ ) is  $\tilde{k} = 2.35 \pm 0.01\text{cm}^{-1}$ . After terminating the carrier, a large-amplitude soliton is injected, which is transmitted through the DSW [45] and the constant region  $A_{\min}$ . Because the soliton speed on the constant region  $A_{\min}$  exceeds the carrier's phase speed ( $\tilde{v}_{\text{ph}} = \tilde{\omega}/\tilde{k}$ ), the soliton overtakes the carrier and forms a new coherent structure. The amplitude of the coherent structure extracted from experiment ( $a_{\text{BB}}(z) = \max_t A(z, t) - A_{\min}$ ) oscillates with propagation. In Fig. 1c, we plot  $a_{\text{BB}}(z)$ , its envelope, and the carrier's properties extracted from each spatial slice of Fig. 1b to characterize propagation up the conduit. The amplitude, mean, and frequency of the carrier and the coherent structure's amplitude envelope exhibit small fluctuations with height  $z$ . We conclude that the coherent structure is a BB consisting of the nonlinear superposition of a soliton and a cnoidal-like wave.

Next, we extract the BB's maximum value for  $\tilde{z} \gtrsim 40\text{cm}$  in Fig. 1b that follows a zig-zag path with constant speed regularly interspersed between regions of rapid acceleration/deceleration. The BB speed across the entire zig-zag path is  $\tilde{v}_{\text{BB}} = 0.63 \pm 0.01\text{cm/s}$  [40], which exceeds the measured carrier phase speed  $\tilde{v}_{\text{ph}} = 0.319 \pm 0.005\text{cm/s}$ . This is consistent with KdV BB solutions [29]. A more thorough analysis of the BB trajectory [40] shows that it can also be viewed as a soliton undergoing a sequence of phase shifts while interacting with a soliton train that composes the cnoidal-like wave [46].

In Fig. 1d, we extract experimental time and spatial slices of  $A(z, t)$ . The measured BB's phase shift in space and time  $\Delta\theta \in (-\pi, \pi]$  is defined as the difference between the left and right carrier phases. We find that  $\Delta\theta_{\text{BB}z} = 0.72\pi$  in space and  $\Delta\theta_{\text{BB}t} = 0.75\pi$  in time are comparable, as expected. This *topological* BB with a positive phase shift is consistent with large amplitude BB solutions of the KdV equation [29].

To generate a DB, the cnoidal-like carrier is set to overtake the soliton. So that the carrier fully absorbs the soliton, it is essential to increase the mean flow rate of the carrier relative to the soliton. This approach is reported in Fig. 2a,b where, now, soliton-cnoidal-like wave interaction results in a depression defect, a DB. For each fixed  $z$ , we define the DB amplitude  $a_{\text{DB}}(z)$  as the difference between the maximum of the carrier and the minimum of the DB upper envelope. The measured averaged carrier parameters are given in Fig. 2c and  $\tilde{k} = 1.95 \pm 0.03\text{cm}^{-1}$ . In contrast to the BB case, the carrier frequency shown in Fig. 2c increases up the conduit. The carrier with a

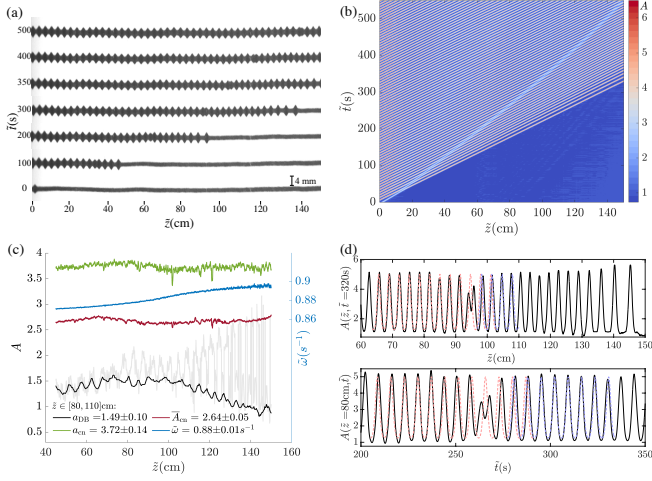


FIG. 2. Absorption of a solitary wave by a larger-mean, larger-amplitude cnoidal-like periodic traveling wave resulting in a dark breather. (a) 90° clockwise rotated time-lapse images. (b) Space-time contour. (c) Background cnoidal-like wave and DB measurements. (d) Spatial and temporal profiles (black solid) and the cnoidal-like wave solution of (1) corresponding to measured parameters (dashed).

larger mean than the soliton leads to more carrier fluctuations than in the BB case. Near the top of the conduit, we observe a 5% increase in the carrier mean and a corresponding change in other DB properties. Generally, the injected interior fluid is suspended at the top after rising through the exterior fluid. We attribute DB modulations for  $\tilde{z} > 110\text{cm}$  to the slow diffusion of interior fluid from the top, which lowers the exterior fluid's density  $\rho_e$ . The observed 5% mean increase can be explained by a correspondingly small 2.5% decrease in the exterior to interior density difference via the Hagen-Poiseuille law in which  $\bar{A} \propto (\rho_e - \rho_i)^{-1/2}$  [39]. Note that a similar mean increase near the top is observed for the BB in Fig. 1c. Despite this, propagation of the DB is robust over a large portion of the conduit  $\tilde{z} \in [80, 110]\text{cm}$  where carrier and DB fluctuations are modest.

The measured DB speed is  $\tilde{v}_{\text{DB}} = 0.27 \pm 0.01\text{cm/s}$  over  $\tilde{z} \in [80, 110]\text{cm}$  while the carrier phase speed is larger  $\tilde{v}_{\text{ph}} = 0.45 \pm 0.01\text{cm/s}$ , a characteristic feature of KdV DBs [29]. Figure 2d shows spatial, temporal slices and the determination of the carrier phase shift. The phase shifts are  $\Delta\theta_{\text{DBz}} = 0.24\pi$  in space and  $\Delta\theta_{\text{DBt}} = 0.25\pi$  in time.

While qualitative features of observed BBs and DBs agree with KdV theory, it is an applicable model for small amplitude only. Therefore, we perform numerical simulations of the strongly nonlinear conduit equation (1) with periodic boundary conditions and an initial condition extracted from the time sliced experimental sections in Figs. 1d and 2d. Figure 3 depicts a comparison of the simulations, experiment, and a KdV breather with fitted carrier and phase shift in the comoving reference

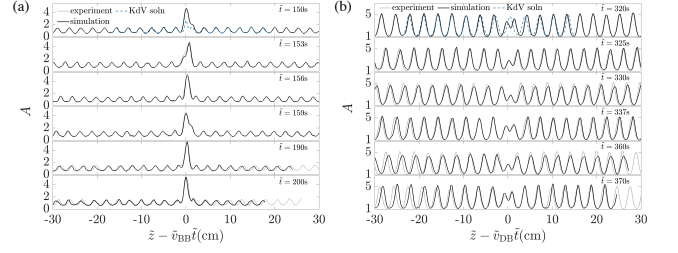


FIG. 3. Experiment (light gray) compared with simulation (black) with initial conditions from experiment, and the KdV breather solution (blue). (a) BB from Fig. 1d. (b) DB from Fig. 2d. The top four panels in (a,b) present the evolution over one period.

frame [40]. In Fig. 3a, an oscillation period of the BB ( $\tilde{T}_{\text{BB}} = 2\pi/(\tilde{v}_{\text{BB}}k - \tilde{\omega}) \approx 9\text{s}$ ) is shown in the top four panels with the, much smaller than observation, KdV BB solution. Viewed as a soliton-soliton train interaction, the BB exhibits the unimodal interaction geometry according to the Lax categories of two-soliton interactions [47–49]. For longer times, the simulation and experiment agree very well, demonstrating the stability, robustness, and accuracy of conduit BBs relative to observation. Small carrier discrepancies are due to unphysical periodic boundary conditions and the acknowledged diffusion issues. The DB in Fig. 3b has period of oscillation  $\tilde{T}_{\text{DB}} = 2\pi/(\tilde{\omega} - \tilde{v}_{\text{DB}}k) \approx 17\text{s}$ , depicted in the top four panels. The dimensional time scale  $T$  from eq. (1) used here is 5% smaller than the nominal, measured  $T$  extracted from separate linear wave measurements [40]. We attribute this discrepancy to interior fluid diffusion and limitations of the conduit equation as a model [34]. The KdV DB solution differs from observation, which exhibits a bimodal interaction according to the Lax categories [49]. The DB simulation closely tracks experiment subject to some carrier discrepancies.

The reliable creation of single topological BBs and DBs in viscous fluid conduits enables the investigation of breather interactions. We create multiple breathers on a fixed carrier background by nonlinear superposing the periodic wavetrain with two solitons of differing amplitude. Figure 4a depicts the interaction of two BBs. The BB created from the larger-amplitude soliton travels at a faster speed and overtakes the smaller amplitude BB. Both BBs are observed to propagate coherently before and after interaction, maintaining essentially the same shape. Figure 4b tracks BB peak trajectories. We separately fit the trajectories before and after interaction with linear functions to derive BB speeds  $\tilde{v}_j$  and spatial shifts  $\Delta\tilde{z}_j$  ( $j = 1, 2$ ) occurring as a result of the interaction (see Tab. I). For each BB, the speeds pre and post interaction are the same, within very small error tolerances, indicating that BB-BB interaction is elastic. The faster (slower) BB experiences a positive (negative) spatial shift.

Figure 4c presents DB interaction. The larger ampli-

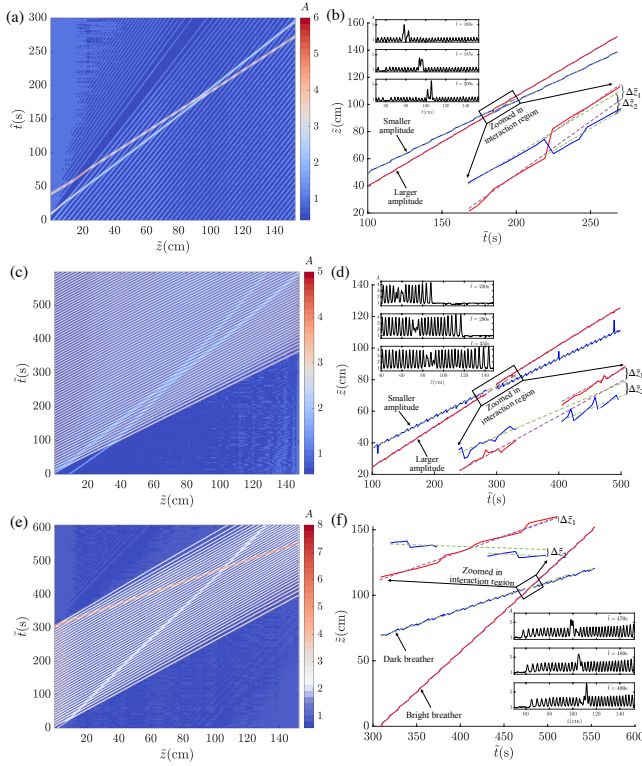


FIG. 4. Observation of breather interactions on a fixed carrier background. (a,c,e) Space-time contour revealing conduit dynamics. (b,d,f) Breather trajectories (blue and red solid) in the  $z$ - $t$  plane with linear fits (dashed) and spatial shifts  $\Delta z_j$ . Subfigures provide representative spatial profiles at specific times. (a,b) BB-BB interaction. (c,d) DB-DB interaction. (e,f) BB-DB interaction.

tude DB originating from the larger amplitude soliton moves faster than the smaller amplitude, slower DB. Trajectories in Fig. 4d trace the positions of the DB upper envelope minima. Again, DB spatial shifts are observed and DB speeds pre and post interaction are conserved (Tab. I). The faster (slower) DB undergoes a positive (negative) spatial shift.

Since all BBs (DBs) are faster (slower) than the carrier, a BB must overtake a DB for them to interact as shown in Fig. 4e. The carrier must have finite spatial extent in order to concurrently overtake and be overtaken by a soliton to create a BB and DB. The speed measurements of BB, DB trajectories (Tab. I) depicted in Fig. 4f again indicate that the interaction is elastic. The DB spatial shift is negative but the positive BB spatial shift is an order of magnitude smaller, hence the BB is scarcely affected by the DB. In all cases of observed topological breather interactions, we find that they are elastic and faster (slower) breathers experience a positive (negative) spatial shift due to the interaction. This observation is consistent with KdV breather interactions characterized in [28].

In Fig. 4, we launch breather pairs on the same car-

rier background. By considering each breather independently, we can infer their nonlinear dispersion relation. In Fig. 4a, individual BB phase shifts after interaction are  $\Delta\theta_{BB1} = -1.08\pi$  and  $\Delta\theta_{BB2} = -0.85\pi$ . Note that it is standard for a phase shift below  $-\pi$  to be shifted to  $(0, \pi)$  by adding a  $2\pi$  period. However, by maintaining the phase shift sign, we can deduce that an increasing BB speed corresponds to an increasing BB amplitude and *decreasing* BB phase shift. This is consistent with the KdV BB dispersion relation [29, 40]. In Fig. 4c, we measure the DB phase shifts post interaction to be  $\Delta\theta_{DB1} = 0.61\pi$  and  $\Delta\theta_{DB2} = 0.52\pi$ . An increasing DB speed corresponds to an increasing DB amplitude and phase shift. For KdV DBs, there are two branches of the DB nonlinear dispersion relation, fast and slow [29, 40]. Our experimental observations are qualitatively consistent with the nonlinear dispersion relation's slow branch of KdV DBs.

This work experimentally verifies that topological breathers can be generated from the interaction of solitons and periodic cnoidal-like traveling waves. While special data analysis techniques have been developed to extract this type of information from complex signals using nonlinear Fourier analysis [13, 50], we have physically realized this nonlinear superposition principle with a simple method. We demonstrate the existence of topological breathers of both bright and dark varieties in a fluid system. All possible breather interactions are observed to be physically elastic (topology and energy conserving) while exhibiting a spatial shift. This work lays the foundation for exploring more complex coherent, topological breather trains and incoherent, far-from-equilibrium breather gases [13, 17, 51].

The authors would like to thank the Isaac Newton Institute for Mathematical Sciences, Cambridge, for support and hospitality during the programme *Dispersive hydrodynamics: mathematics, simulation and experiments, with applications in nonlinear waves*, where work on this paper was discussed. This work was supported by NSF DMS-1816934.

\* yifeng.mao@colorado.edu

- [1] L. F. Mollenauer, R. H. Stolen, and J. P. Gordon, Experimental Observation of Picosecond Pulse Narrowing and Solitons in Optical Fibers, *Phys. Rev. Lett.* **45**, 1095 (1980).
- [2] A. Weiner, J. Heritage, R. Hawkins, R. Thurston, E. Kirschner, D. Leaird, and W. Tomlinson, Experimental observation of the fundamental dark soliton in optical fibers, *Physical review letters* **61**, 2445 (1988).
- [3] D. Mandelik, H. S. Eisenberg, Y. Silberberg, R. Morandotti, and J. S. Aitchison, Observation of Mutually Trapped Multiband Optical Breathers in Waveguide Arrays, *Phys. Rev. Lett.* **90**, 253902 (2003).
- [4] A. Chabchoub, O. Kimmoun, H. Branger, N. Hoffmann,



	Breather 1			Breather 2		
	$\tilde{v}_1$ before (cm/s)	$\tilde{v}_1$ after (cm/s)	$\Delta\tilde{z}_1$ (cm)	$\tilde{v}_2$ before (cm/s)	$\tilde{v}_2$ after (cm/s)	$\Delta\tilde{z}_2$ (cm)
BB-BB	$0.65 \pm 0.01$	$0.64 \pm 0.01$	2.69	$0.55 \pm 0.01$	$0.53 \pm 0.01$	-1.54
DB-DB	$0.25 \pm 0.01$	$0.24 \pm 0.01$	1.75	$0.20 \pm 0.01$	$0.19 \pm 0.01$	-1.97
BB-DB	$0.61 \pm 0.01$	$0.62 \pm 0.01$	0.15	$0.22 \pm 0.01$	$0.21 \pm 0.01$	-1.22

TABLE I. Speed and spatial shift measurements of breather interactions.

- D. Proment, M. Onorato, and N. Akhmediev, Experimental observation of dark solitons on the surface of water, *Physical review letters* **110**, 124101 (2013).
- [5] R. Pethiyagoda, S. W. McCue, and T. J. Moroney, Spectrograms of ship wakes: Identifying linear and nonlinear wave signals, *J. Fluid Mech.* **811**, 189 (2017).
- [6] R. Grimshaw, J. C. B. da Silva, and J. M. Magalhaes, Modelling and observations of oceanic nonlinear internal wave packets affected by the Earth's rotation, *Ocean Modelling* **116**, 146 (2017).
- [7] R. W. Boyd, *Nonlinear Optics* (Academic Press, 2013).
- [8] C. Kharif, E. N. Pelinovskii, and A. Slunyaev, *Rogue Waves in the Ocean*, Advances in Geophysical and Environmental Mechanics and Mathematics (Springer, Berlin, 2009).
- [9] B. Kibler, J. Fatome, C. Finot, G. Millot, F. Dias, G. Genty, N. Akhmediev, and J. M. Dudley, The Peregrine soliton in nonlinear fibre optics, *Nature Phys* **6**, 790 (2010).
- [10] A. Chabchoub, N. Hoffmann, and N. Akhmediev, Rogue wave observation in a water wave tank, *Physical Review Letters* **106**, 204502 (2011).
- [11] M. N rhi, B. Wetzel, C. Billet, S. Toenger, T. Sylvestre, J.-M. Merolla, R. Morandotti, F. Dias, G. Genty, and J. M. Dudley, Real-time measurements of spontaneous breathers and rogue wave events in optical fibre modulation instability, *Nat Commun* **7**, 13675 (2016).
- [12] A. Tikan, F. Bonnefoy, G. Roberti, G. El, A. Tovbis, G. Ducrozet, A. Cazaubiel, G. Prabhudesai, G. Michel, F. Copie, E. Falcon, S. Randoux, and P. Suret, Prediction and manipulation of hydrodynamic rogue waves via nonlinear spectral engineering, *Phys. Rev. Fluids* **7**, 054401 (2022).
- [13] A. Costa, A. R. Osborne, D. T. Resio, S. Alessio, E. Chiriv , E. Saggese, K. Bellomo, and C. E. Long, Soliton Turbulence in Shallow Water Ocean Surface Waves, *Phys. Rev. Lett.* **113**, 108501 (2014).
- [14] S. Randoux, P. Walczak, M. Onorato, and P. Suret, Intermittency in Integrable Turbulence, *Phys. Rev. Lett.* **113**, 113902 (2014).
- [15] J. M. Soto-Crespo, N. Devine, and N. Akhmediev, Integrable Turbulence and Rogue Waves: Breathers or Solitons?, *Phys. Rev. Lett.* **116**, 103901 (2016).
- [16] A. R. Osborne, D. T. Resio, A. Costa, S. Ponce de Le n, and E. Chiriv , Highly nonlinear wind waves in Currituck Sound: Dense breather turbulence in random ocean waves, *Ocean Dyn.* **69**, 187 (2019).
- [17] G. El and A. Tovbis, Spectral theory of soliton and breather gases for the focusing nonlinear schr dinger equation, *Physical Review E* **101**, 052207 (2020).
- [18] N. Lazarides, M. Eleftheriou, and G. Tsironis, Discrete breathers in nonlinear magnetic metamaterials, *Physical review letters* **97**, 157406 (2006).
- [19] M. Wu, Nonlinear spin waves in magnetic film feedback rings, in *Solid State Physics*, Vol. 62, edited by R. E. Camley and R. L. Stamps (Academic Press, Burlington, 2011) pp. 163–224.
- [20] A. Di Carli, C. D. Colquhoun, G. Henderson, S. Flannigan, G.-L. Oppo, A. J. Daley, S. Kuhr, and E. Haller, Excitation Modes of Bright Matter-Wave Solitons, *Phys. Rev. Lett.* **123**, 123602 (2019).
- [21] D. Luo, Y. Jin, J. H. V. Nguyen, B. A. Malomed, O. V. Marchukov, V. A. Yurovsky, V. Dunjko, M. Olshanii, and R. G. Hulet, Creation and Characterization of Matter-Wave Breathers, *Phys. Rev. Lett.* **125**, 183902 (2020).
- [22] S. Flach and A. V. Gorbach, Discrete breathers — Advances in theory and applications, *Phys. Rep.* **467**, 1 (2008).
- [23] N. Boechler, G. Theocharis, S. Job, P. G. Kevrekidis, M. A. Porter, and C. Daraio, Discrete breathers in one-dimensional diatomic granular crystals, *Physical review letters* **104**, 244302 (2010).
- [24] G. James, Travelling breathers and solitary waves in strongly nonlinear lattices, *Phil. Trans. R. Soc. A.* **376**, 20170138 (2018).
- [25] A. Hasegawa and Y. Kodama, *Solitons in optical communications*, 7 (Oxford University Press on Demand, 1995).
- [26] A. Chabchoub, K. Mozumi, N. Hoffmann, A. V. Babanin, A. Toffoli, J. N. Steer, T. S. van den Bremer, N. Akhmediev, M. Onorato, and T. Waseda, Directional soliton and breather beams, *Proc. Natl. Acad. Sci.* **116**, 9759 (2019).
- [27] E. A. Kuznetsov and A. V. Mikhailov, Stability of stationary waves in nonlinear weakly dispersive media, *Sov. Phys. JETP* **40**, 855 (1975).
- [28] M. Bertola, R. Jenkins, and A. Tovbis, Partial degeneration of finite gap solutions to the korteweg-de vries equation: soliton gas and scattering on elliptic background, *arXiv preprint arXiv:2210.01350* (2022).
- [29] M. A. Hoefer, A. Mucalica, and D. E. Pelinovsky, Kdv breathers on a cnoidal background, *arXiv preprint arXiv:2301.08154* (2023).
- [30] Y. S. Kivshar and B. Luther-Davies, Dark optical solitons: Physics and applications, *Phys. Rep.* **298**, 81 (1998).
- [31] M. J. Ablowitz, *Nonlinear Dispersive Waves: Asymptotic Analysis and Solitons*, 1st ed., Cambridge Texts in Applied Mathematics (Cambridge University Press, Cambridge, UK ; New York, 2011).
- [32] S. Clarke, R. Grimshaw, P. Miller, E. Pelinovsky, and T. Talipova, On the generation of solitons and breathers in the modified Korteweg–de Vries equation, *Chaos* **10**, 383 (2000).
- [33] H. Leblond and D. Mihalache, Models of few optical cycle solitons beyond the slowly varying envelope approximation, *Models of Few Optical Cycle Solitons beyond the Slowly Varying Envelope Approximation*, **523**, 61.
- [34] Y. Mao and M. A. Hoefer, Experimental investigations of linear and nonlinear periodic travelling waves in a viscous fluid conduit, *Journal of Fluid Mechanics* **954**, A14 (2023).

- [35] J. Martin, N. Rakotomalala, D. Salin, L. Talon, *et al.*, Convective/absolute instability in miscible core-annular flow. part 1: Experiments, *Journal of fluid mechanics* **618**, 305 (2009).
- [36] B. Selvam, L. Talon, L. Lesshafft, and E. Meiburg, Convective/absolute instability in miscible core-annular flow. part 2. numerical simulations and nonlinear global modes, *Journal of Fluid Mechanics* **618**, 323 (2009).
- [37] D. R. Scott, D. J. Stevenson, and J. A. Whitehead, Observations of solitary waves in a viscously deformable pipe, *Nature* **319**, 759 (1986).
- [38] P. Olson and U. Christensen, Solitary wave propagation in a fluid conduit within a viscous matrix, *Journal of Geophysical Research: Solid Earth* **91**, 6367 (1986).
- [39] N. K. Lowman and M. A. Hoefer, Dispersive hydrodynamics in viscous fluid conduits, *Physical Review E* **88**, 023016 (2013).
- [40] See Supplemental Material at — for additional mathematical and experimental details.
- [41] M. D. Maiden and M. A. Hoefer, Modulations of viscous fluid conduit periodic waves, *Proceedings of the Royal Society A: Mathematical, Physical and Engineering Sciences* **472**, 20160533 (2016).
- [42] K. R. Helfrich and J. A. Whitehead, Solitary waves on conduits of buoyant fluid in a more viscous fluid, *Geophysical & Astrophysical Fluid Dynamics* **51**, 35 (1990).
- [43] M. D. Maiden, N. K. Lowman, D. V. Anderson, M. E. Schubert, and M. A. Hoefer, Observation of dispersive shock waves, solitons, and their interactions in viscous fluid conduits, *Physical review letters* **116**, 174501 (2016).
- [44] S. Gavrilyuk and K.-M. Shyue, Singular solutions of the BBM equation: analytical and numerical study, *Nonlinearity* **35**, 388 (2021).
- [45] M. D. Maiden, D. V. Anderson, N. A. Franco, G. A. El, and M. A. Hoefer, Solitonic dispersive hydrodynamics: theory and observation, *Physical review letters* **120**, 144101 (2018).
- [46] G. B. Whitham, Comments on periodic waves and solitons, *IMA J. Appl. Math.* **32**, 353 (1984).
- [47] P. D. Lax, Integrals of nonlinear equations of evolution and solitary waves, *Commun. Pure Appl. Math.* **21**, 467 (1968).
- [48] W. Craig, P. Guyenne, J. Hammack, D. Henderson, and C. Sulem, Solitary water wave interactions, *Phys. Fluids* **18**, 057106 (2006).
- [49] N. K. Lowman, M. A. Hoefer, and G. A. El, Interactions of large amplitude solitary waves in viscous fluid conduits, *Journal of fluid mechanics* **750**, 372 (2014).
- [50] M. Brühl, P. J. Prins, S. Ujvary, I. Barranco, S. Wahls, and P. L. F. Liu, Comparative analysis of bore propagation over long distances using conventional linear and KdV-based nonlinear Fourier transform, *Wave Motion* **111**, 102905 (2022).
- [51] G. A. El, Soliton gas in integrable dispersive hydrodynamics, *J. Stat. Mech.* **2021**, 114001 (2021).

# Supplemental Material for "Creation and Interaction of Dark and Bright Topological Breathers from Soliton-Cnoidal Wave Collisions"

Yifeng Mao,<sup>1,\*</sup> Sathyanarayanan Chandramouli,<sup>2</sup> Wenqian Xu,<sup>1</sup> and Mark Hoefer<sup>1</sup>

<sup>1</sup> *Department of Applied Mathematics, University of Colorado, Boulder, CO 80309, USA*

<sup>2</sup> *Department of Mathematics, Florida State University, Tallahassee, FL 32306, USA.*

(Dated: February 23, 2023)

## I. EXPERIMENTAL SETUP AND METHOD

The experiments are conducted in a 180 cm tall square acrylic column with a cross-sectional area of  $5 \times 5 \text{ cm}^2$  (see Fig. S1 for a schematic illustration). The column is filled with high-viscosity pure glycerin as the exterior fluid, and the interior fluid, made of a mixture of glycerin ( $\sim 70\%$ ), water ( $\sim 20\%$ ), and black food coloring ( $\sim 10\%$ ), which is less viscous and dense, is injected into the column using a computer-controlled piston pump. Table S1 reports nominal fluid properties. The interior fluid rises to the top and forms a floating thin layer that very slowly diffuses. We focus on the dynamics of the two-Stokes fluids' interface away from the top and consider the wavemaker problem with only one boundary condition at the injection site. Prior to imaging, a straight conduit is created by the steady injection rate

$$Q^{(i)}(t) = Q_0 q(t), \quad q(t) = 1,$$

where the superscript  $(i)$  represents quantities for the interior fluid,  $q(t)$  is a time-dependent dimensionless boundary condition, and  $Q_0$  is a constant injection rate. We obtain various interfacial wave dynamics by programming the injection rate  $q(t)$ .

The conduit interfacial waves are imaged by a high-resolution digital camera with a sample rate of 2 Hz for Fig. 1 of the main text and 1 Hz for the remaining datasets. The camera is positioned slightly above the injection boundary and captures the interfacial waves in a fully established conduit. We identify the starting point in the camera view as  $z = 0$  and the imaging starting time as  $t = 0$ . Conduit diameters  $D$  are extracted by measuring the local extrema of centered differences of grayscale images in the direction normal to the interface. Conduit diameters approximately follow the Hagen-Poiseuille relation  $D = \alpha Q^{(i)1/4}$  [S1, S2], where  $\alpha = (2^7 \mu^{(i)})^{1/4} / (\pi g \Delta)$ ,  $\mu^{(i)}$  is the interior viscosity,  $g$  is the acceleration due to gravity and  $\Delta = \rho^{(e)} - \rho^{(i)}$  is the difference in the exterior and interior densities. However, as reported in [S3], the conduit diameter in the upper portion of the fluid column is found to be slightly larger than that near the bottom, which leads to changes in the interfacial wave profiles as discussed in the main text.

The normalized conduit cross-sectional area  $A$  is obtained as  $A = (D/D_0)^2$ , where  $D_0$  is the constant conduit diameter at the steady injection rate  $q_0$ . The initial-boundary value conditions for the wavemaker problem in terms of the conduit interfacial area  $A$  are

$$\begin{aligned} A(z, 0) &= 1, \quad z \geq 0, \\ A(0, t) &= f(t), \quad t \geq 0, \end{aligned}$$

where  $f(t) = q(t)^{1/2}$ .

Determination of the nondimensionalization scales  $L, U$  and  $T = L/U$  utilizes the method discussed in [S4]. After setting up each experiment, we generate trials of linear periodic waves in the fluid conduit and measure their dimensional wavenumber  $\tilde{k}$  (rad/cm) and frequency  $\tilde{\omega}_0$  (rad/s). Fitting  $(\tilde{k}, \tilde{\omega})$  with the conduit equation linear dispersion relation

$$\tilde{\omega} = \frac{2U\tilde{k}}{1 + L^2\tilde{k}^2},$$

we obtain the vertical length scale  $L$  (cm) and velocity scale  $U$  (cm/s). The corresponding time scale is  $T = L/U$  (s). The resulting scales for each experiment of the main text are reported in Table S2.

## II. GENERATION OF SOLITONS AND CNOIDAL-LIKE PERIODIC TRAVELING WAVES

Viscous fluid conduit interfacial waves have been shown to exhibit solitons that stably propagate along the conduit with constant speed and possess physical elasticity (speed conservation) after interaction with another soliton [S5, S6].

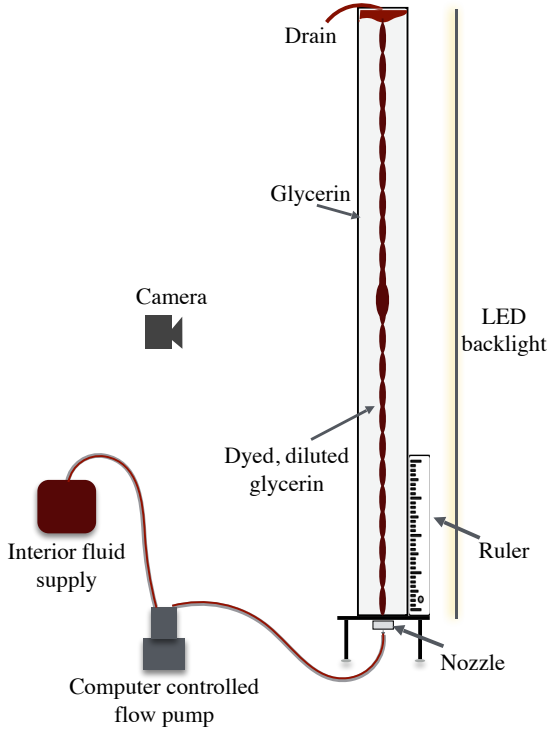


FIG. S1: Schematic of the experimental apparatus.

TABLE S1: Example fluid properties (measured in the experiment of Fig. 1): viscosities  $\mu^{(i,e)}$ , viscosity ratio  $\epsilon$ , densities  $\rho^{(i,e)}$ , background flow rate  $Q_0$ , associated conduit diameter  $D_0$  computed by Poiseuille's law, outer wall diameter  $D_{\text{out}}$ , and Reynolds numbers  $Re^{(i,e)}$  for interior and exterior fluids.

$\mu^{(i)}$	0.045 Pa s
$\mu^{(e)}$	1.10 Pa s
$\epsilon$	0.041
$\rho^{(i)}$	1.21 g cm <sup>-3</sup>
$\rho^{(e)}$	1.26 g cm <sup>-3</sup>
$Q_0$	1.00 cm <sup>3</sup> min <sup>-1</sup>
$D_0$	0.56 cm
$D_{\text{out}}$	5.00 cm
$Re^{(i)}$	0.21
$Re^{(e)}$	0.0087
Camera resolution 39.36 pix cm <sup>-1</sup>	

Fig	Carrier wave						Scales	
	region	$a$	$\omega$	$k$	$A$	$k_n(a, \omega, A)$	$L$ (cm)	$T$ (s)
Fig. 1b	$z \in [40, 100]\text{cm}, t \in [1, 50]\text{s}$	$0.94 \pm 0.08$	$0.71 \pm 0.05$	$0.42 \pm 0.02$	$1.00 \pm 0.03$	0.43	$0.18 \pm 0.01$	$0.95 \pm 0.06$
Fig. 2b	$z \in [80, 110]\text{cm}, t \in [400, 500]\text{s}$	$3.72 \pm 0.14$	$1.21 \pm 0.08$	$0.31 \pm 0.02$	$2.64 \pm 0.05$	0.33	$0.16 \pm 0.01$	$1.38 \pm 0.09$
Fig. 4a	$z \in [100, 140]\text{cm}, t \in [1, 100]\text{s}$	$0.96 \pm 0.07$	$0.68 \pm 0.04$	$0.39 \pm 0.02$	$1.00 \pm 0.04$	0.40	$0.18 \pm 0.01$	$0.95 \pm 0.06$
Fig. 4c	$z \in [40, 70]\text{cm}, t \in [300, 500]\text{s}$	$2.98 \pm 0.19$	$1.22 \pm 0.08$	$0.36 \pm 0.02$	$2.31 \pm 0.04$	0.39	$0.19 \pm 0.01$	$1.55 \pm 0.10$
Fig. 4e	$z \in [100, 120]\text{cm}, t \in [400, 450]\text{s}$	$2.52 \pm 0.16$	$1.25 \pm 0.07$	$0.37 \pm 0.02$	$2.40 \pm 0.05$	0.36	$0.15 \pm 0.01$	$1.43 \pm 0.08$

TABLE S2: Nondimensional carrier wave parameters for each reported experiment in the main text. Column 2: selected windows for measurements. Columns 3-6: measured wave parameters. Column 7: numerically computed solution  $k_n$  at measured  $(a, \omega, A)$ , compared with measured  $k$ . Columns 8,9: nondimensionalization vertical length and time scales.

Experimental generation of solitons in a conduit uses pre-computed soliton solutions of the conduit equation  $f(t) = a_{\text{sol}}(-c_{\text{sol}}(t - t_0))$ , where  $c_{\text{sol}} = (1 + a_0^2(2 \ln a_0 - 1))/(a_0 - 1)^2$  is the wave speed,  $a_0 = a_{\text{sol}}(0)$  is the soliton amplitude, and  $a_{\text{sol}}(z)$  is the soliton profile.

Conduit periodic traveling wave solutions satisfying  $A(z, t) = g(\theta)$ ,  $\theta = kz - \omega t$ ,  $g(\theta + 2\pi) = g(\theta)$  for  $\theta \in \mathbb{R}$  exhibit cnoidal-like patterns in the strongly nonlinear regime. In experiments, we use pre-computed conduit periodic traveling wave solutions  $f(t) = g(-\omega t)$  to launch waves from the boundary. The wave propagating into a quiescent, straight conduit is subject to a developing dispersive modulation region. It is stabilized after sustained, periodic injection, at which time a periodic conduit is established. Investigation of its reliable creation and agreement with the conduit equation nonlinear dispersion relation have been realized in [S4]. Table S2 presents the averaged cnoidal-like carrier wave parameters extracted over a window of each reported dataset. Windows of measurement are chosen to focus on the periodic region solely. We scaled the bright breathers (BBs) to have unit mean since the soliton and the carrier wave are on the same mean. On the other hand, we did not perform such scaling for the dark breathers (DBs) since the DBs were intentionally created by interacting two waves with different means. The cnoidal-like wavetrain is subject to a larger wave amplitude  $a = A_{\text{max}} - A_{\text{min}}$  and a larger wave mean  $\bar{A}$ . The wavenumber is obtained as  $k = 2\pi/l$ , where  $l$  is the averaged wavelength in the spatial domain, and the frequency is  $\omega = 2\pi/p$ , where  $p$  is the averaged wave period in the temporal domain.



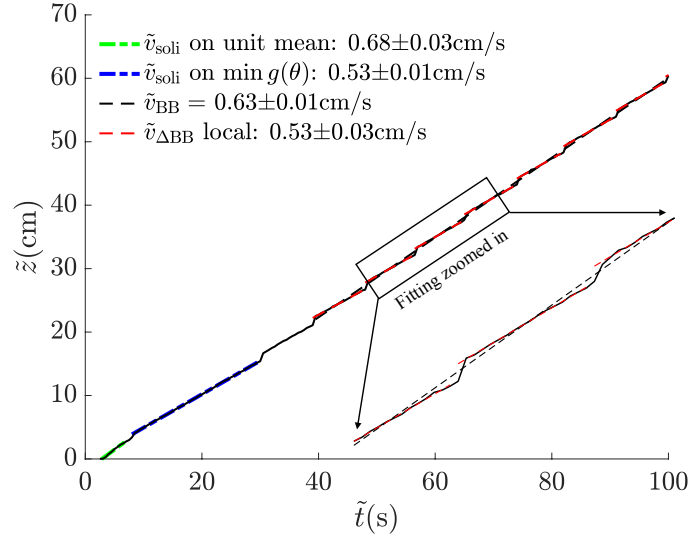


FIG. S2: Comparison of speeds for the topological BB in Fig. 1b of the main text and the soliton before interacting with the carrier. The space-time trajectory is fitted with linear functions for each sector, and the colors correspond to the different states of the soliton and the BB.

### III. SPEED OF THE BRIGHT BREATHER

The topological BB in Fig. 1b of the main text consists of a soliton overtaking a cnoidal-like periodic carrier wave, both of which are on unit mean. We now investigate the BB speed, compared with the associated soliton speed before interacting with the cnoidal-like carrier. In Fig. S2, we track the trajectory of the BB by extracting the position of the breather peak at each time slice.

We consider the trajectory in three regions. The fitted green curve in Fig. S2 presents the speed of the soliton on unit mean. The soliton then propagates into a constant state  $A_{\min}$  that connects the unit mean and the minimum of the adjacent, localized carrier wave  $A(z, t) = g(\theta)$ ,  $\theta = kz - \omega t$ . The speed of soliton propagation in this region is fitted in blue in Fig. S2. A BB is constructed after  $\tilde{t} \approx 40$  s when the soliton penetrates the carrier, tracked in black. As explained in the main text, the BB follows a zig-zag path with constant speeds in between the spatial shifts. We, therefore, obtain the breather's *local speed*  $\tilde{v}_{\text{BB}}$  by fitting the local trajectories in between each spatial shift. The speed of the BB across the entire zig-zag path is  $\tilde{v}_{\text{BB}} = 0.63 \pm 0.01$  cm/s, faster than the averaged local speed  $\tilde{v}_{\text{BB}} = 0.53 \pm 0.03$  cm/s because of the forward spatial shifts. We also observe that the soliton on unit mean (green) has a faster speed than that on the constant, lower state  $A_{\min}$  (blue), as expected. More importantly, the soliton on the constant state  $A_{\min}$  has speed  $\tilde{v}_{\text{sol}} = 0.53 \pm 0.01$  cm/s, the same as the averaged BB local speed  $\tilde{v}_{\text{BB}}$ , implying that the periodic carrier wave can be interpreted as a soliton train and the interaction of the soliton with the carrier consists of free propagation followed by an elastic interaction spatial shift periodically repeated.

### IV. COMPARISON OF CONDUIT BREATHERS WITH KDV BREATHER SOLUTIONS

In [S7], two varieties of exact, topological breather solutions of the Korteweg-de Vries (KdV) equation - bright and dark - are obtained, representing soliton-cnoidal wave interactions. These breathers impart a phase shift to the cnoidal wave. Herein, we compare both topological bright and dark breathers from conduit experiments with the KdV breather solutions by selecting a KdV solution that possesses the same cnoidal background and the same phase shift as the experimental data. Before that, we first need to derive the KdV equation from the conduit equation in the weakly nonlinear, long-wavelength regime.

The conduit equation

$$A_t + (A^2)_z - (A^2(A^{-1}A_t)_z)_z = 0, \quad (1)$$

can be reduced to the KdV equations for  $T = \delta^{1/2}t$ ,  $Z = \delta^{1/2}z$ , and  $A(z, t) = 1 + \delta u(Z, T)$ ,  $\delta \ll 1$ . Insertion of this ansatz into (1) and keeping the leading and first-order terms results in the Benjamin-Bona-Mahony (BBM) equation

$u_T + 2u_Z + 2\delta uu_Z - \delta u_{ZZT} = 0$ . Since  $u_T = -2u_Z + \mathcal{O}(\delta)$ ,  $u_{ZZT} = -2u_{ZZZ} + \mathcal{O}(\delta)$  so that  $u_T + 2u_Z + 2\delta uu_Z + 2\delta u_{ZZZ} = 0$  to the same order of accuracy. Hence, both the BBM and KdV equations are asymptotically equivalent to the conduit equation (1) in the weakly nonlinear, long wavelength regime. Taking  $\delta = 1$ , we arrive at the unscaled KdV equation

$$u_t + 2u_z + 2uu_z + 2u_{zzz} = 0. \quad (2)$$

Letting  $u(z, t) = 6v(x, \tau)$ , where  $x = z - 2t$  and  $\tau = 2t$ , (2) is scaled into the normalized form

$$v_\tau + 6vv_x + v_{xxx} = 0 \quad (3)$$

as given in [S7], which possesses the normalized cnoidal solution  $v(x, \tau) = 2mcn^2(x - c_0\tau, m)$ , where  $m$  is the elliptic parameter of the Jacobi elliptic cosine function and  $c_0 = 4(2m - 1)$  is the speed. Know that the KdV equation is subject to the scaling symmetry  $\tilde{v} = \mu^2 v$ ,  $\tilde{x} = \frac{x}{\mu}$ ,  $\tilde{\tau} = \frac{\tau}{\mu^3}$ , where  $\mu > 0$  and a Galilean boost so that the solution can be shifted to zero mean. We obtain the scaled, shifted cnoidal wave solution of the KdV equation (2) on zero mean

$$u(z, t) = -6\bar{u} + 12m\mu^2 cn^2[\mu(z - 2(1 - 6\bar{u} + c_0\mu^2)t), m], \quad (4)$$

where  $\bar{u} = \frac{2m\mu^2}{K(m)} \int_0^{K(m)} cn^2(x, m) dx = 2\mu^2 (E(m)/K(m) - (1 - m))$ . In addition, the conduit solution  $A(z, t) = 1 + u(z, t)$  admits the scaling  $A^* = \bar{A}A$ ,  $z^* = \bar{A}^{1/2}z$ ,  $t^* = \bar{A}^{-1/2}t$  that leaves (1) invariant, where  $\bar{A} > 0$ . Here we use asterisks to refer to the solution on mean  $\bar{A}$ . Applying this scaling invariance to (4), we obtain the approximate cnoidal solution of the conduit equation

$$A^*(z^*, t^*) = \bar{A}(1 - 6\bar{u}) + acn^2\left[\frac{\sqrt{a}}{\bar{A}\sqrt{12m}}\left(z^* - 2\left(\bar{A} - 6\bar{A}\bar{u} + \frac{a(2m-1)}{3m}\right)t^*\right), m\right], \quad (5)$$

where  $\bar{u} = \frac{a}{6\bar{A}m} (E(m)/K(m) - (1 - m))$ . The solution (5) has mean  $\bar{A}$ , amplitude  $a$ , wavenumber  $k = \frac{\pi\sqrt{a}}{K(m)\bar{A}\sqrt{12m}}$  and phase speed  $C_0 = 2\left(\bar{A} - 6\bar{A}\bar{u} + \frac{a(2m-1)}{3m}\right)$ . The corresponding frequency is given by  $\omega = C_0 k$ . We now fit (5) to experiment by measuring  $(a, \bar{A}, k)$  to determine  $m$ .

The top panels in Fig. 3 of the main text present comparisons of the BB and DB from experiment and the KdV breather solutions approximated in the same way. The normalized KdV equation (3) admits BB and DB solutions in the form [S7]

$$v(x, \tau) = 2\left[m - 1 + \frac{E(m)}{K(m)}\right] + 2\partial_x^2 \log \nu(x, \tau),$$

where the  $\nu$ -function for the BB is given by

$$\nu(x, \tau) := \Theta(x - c_0\tau + \alpha_b)e^{\kappa_b(x - c_b\tau + x_0)} + \Theta(x - c_0\tau - \alpha_b)e^{-\kappa_b(x - c_b\tau + x_0)}$$

with breather speed  $c_b > c_0$ , inverse width  $\kappa_b$  and phase shift  $-2\alpha_b \in (-2K(m), 0]$ , and the  $\nu$ -function for the DB is given by

$$\nu(x, \tau) := \Theta(x - c_0\tau + \alpha_d)e^{-\kappa_d(x - c_d\tau + x_0)} + \Theta(x - c_0\tau - \alpha_d)e^{\kappa_d(x - c_d\tau + x_0)},$$

with breather speed  $c_d < c_0$ , inverse width  $\kappa_d$  and phase shift  $2\alpha_d \in [0, 2K(m))$ .  $x_0$  is a spatial shift of the breather relative to the carrier. In Fig. 3a of the main text for the BB comparison, to match the measured nondimensional wave parameters  $(a, \bar{A}, k) = (0.94, 1.00, 0.42)$  requires  $m = 0.82$  in the cnoidal solution (5). The BBs are on the same carrier with phase shift  $\Delta\theta_{BB} = -1.28\pi$ . The amplitude of the KdV BB is nearly half of the conduit BB. The measured carrier phase speed is  $v_{ph} = 1.68$ , compared to the predicted phase speed of the cnoidal solution  $C_0 = 1.74$ . The first panel in Fig. 3b of the main text has carrier wave parameters  $(a, \bar{A}, k) = (3.72, 2.64, 0.31)$  and phase shift  $\Delta\theta_{DB} = 0.24\pi$  for both the experimental DB and the KdV DB solutions. Fitting  $(a, \bar{A}, k)$  to (5) determines  $m = 0.83$ . Similar to the BB comparison, the KdV DB has a smaller amplitude than the conduit DB. The experimental DB exhibits a bimodal structure during a period of oscillation, but the KdV DB is unimodal [S8]. The measured and predicted cnoidal phase speeds are  $v_{ph} = 3.94$  and  $C_0 = 4.33$ , respectively.

The nonlinear dispersion relation of the KdV breathers solutions is given by [S7]

$$\alpha_b = F(\varphi_\gamma, m), \quad \kappa_b = \frac{\sqrt{1 - \lambda - m}\sqrt{-\lambda - m}}{\sqrt{1 - 2m - \lambda}} - Z(\varphi_\gamma, m), \quad c_b = c_0 + \frac{4\sqrt{1 - \lambda - 2m}\sqrt{1 - \lambda - m}\sqrt{-\lambda - m}}{\kappa_b}$$

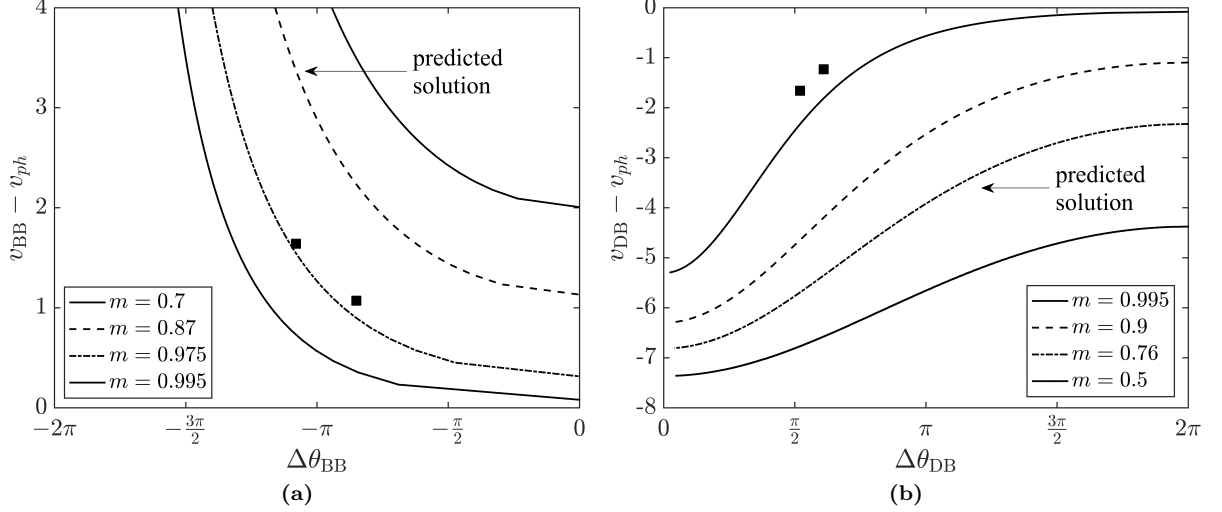


FIG. S3: Representative KdV breather nonlinear dispersion relation curves for the BB (left) and DB (right) solutions. Markers are the measured conduit BB (left) and DB (right) speed-phase shift relation.

for the BB, where  $\varphi_\gamma \in (0, \frac{\pi}{2})$  is found from  $\sin \varphi_\gamma = \frac{\sqrt{-\lambda-m}}{\sqrt{1-2m-\lambda}}$ , and

$$\alpha_d = F(\varphi_\alpha, m), \quad \kappa_d = Z(\varphi_\alpha, m), \quad c_d = c_0 - \frac{4\sqrt{\lambda+m}\sqrt{\lambda-1+2m}\sqrt{1-\lambda-m}}{\kappa_d}$$

for the DB, where  $\varphi \in (0, \frac{\pi}{2})$  is from  $\sin \varphi_\alpha = \frac{\sqrt{1-m-\lambda}}{\sqrt{m}}$ . The normalized phase shift of the background cnoidal wave can be written as

$$\Delta\theta_{BB} = -\frac{2\pi\alpha_b}{K(m)} \in (-2\pi, 0], \quad \Delta\theta_{DB} = \frac{2\pi\alpha_d}{K(m)} \in [0, 2\pi).$$

Figure S3 demonstrates the dependence of breather-phase speed difference versus breather normalized phase shift of the KdV breather solutions. We then compare the BB-BB and DB-DB interaction experiments in Fig.4 of the main text with the KdV breather nonlinear dispersion relation in Fig.S3. The BB-BB interaction in Fig.4a of the main text is on a nondimensional carrier background of  $(a, \bar{A}, k) = (0.96, 1.00, 0.39)$  so that  $m = 0.87$ . The measured cnoidal phase speed is  $v_{ph} = 1.74$ , while the predicted is  $C_0 = 1.81$ . The BB speeds and phase shifts are  $(v_1, \Delta\theta_1) = (3.38, -1.08\pi)$ ,  $(v_2, \Delta\theta_2) = (2.81, -0.85\pi)$ . In Fig. S3a, we plot the observed BBs' breather-phase speed differences against their phase shifts. The predicted solution corresponds to the curve at  $m = 0.87$ , but we observe that the experimental BB lies on the curve at  $m = 0.975$ . This means that if we fix the carrier background for the same phase shift, the experimental BB has a smaller breather-phase speed difference than the approximate KdV BB. Nevertheless, our conduit BB-BB interaction experiment agrees qualitatively with the KdV breather nonlinear dispersion relation since an increasing BB speed corresponds to an increasing BB amplitude and *decreasing* BB phase shift.

On the other hand, the DB-DB interaction in Fig.4c of the main text is on a carrier of  $(a, \bar{A}, k) = (2.98, 0.36, 2.31)$ , implying  $m = 0.76$ . Again, we obtain the measured and predicted carrier phase speeds  $v_{ph} = 3.39$  and  $C_0 = 4.71$ , respectively. The measured DB properties are  $(v_1, \Delta\theta_1) = (2.16, 0.61\pi)$ ,  $(v_2, \Delta\theta_2) = (1.73, 0.52\pi)$ . In Fig. S3b, we find the speed-phase shift relation of the experimental DBs is close to the KdV nonlinear dispersion relation at  $m = 0.995$ . Qualitative agreement is achieved with the KdV prediction since an increasing DB speed corresponds to an increasing DB phase shift.

\* Electronic address: yifeng.mao@colorado.edu

[S1] J. A. Whitehead Jr and D. S. Luther, Journal of Geophysical Research **80**, 705 (1975).

[S2] D. R. Scott, D. J. Stevenson, and J. A. Whitehead, Nature **319**, 759 (1986).

[S3] M. D. Maiden, N. K. Lowman, D. V. Anderson, M. E. Schubert, and M. A. Hoefer, Physical review letters **116**, 174501 (2016).

- [S4] Y. Mao and M. A. Hoefer, *Journal of Fluid Mechanics* **954**, A14 (2023).
- [S5] P. Olson and U. Christensen, *Journal of Geophysical Research: Solid Earth* **91**, 6367 (1986).
- [S6] K. R. Helfrich and J. A. Whitehead, *Geophysical & Astrophysical Fluid Dynamics* **51**, 35 (1990).
- [S7] M. A. Hoefer, A. Mucalica, and D. E. Pelinovsky, *arXiv preprint arXiv:2301.08154* (2023).
- [S8] N. K. Lowman, M. A. Hoefer, and G. A. El, *Journal of fluid mechanics* **750**, 372 (2014).